https://doi.org/10.1038/s41586-019-1226-z

Epitaxial growth of a 100-square-centimetre single-crystal hexagonal boron nitride monolayer on copper

Li Wang[1,2,18], Xiaozhi Xu[1,18], Leining Zhang[3,4,18], Ruixi Qiao[1,18], Muhong Wu[1,5], Zhichang Wang[6], Shuai Zhang[7], Jing Liang[1], Zhihong Zhang[1], Zhibin Zhang[1], Wang Chen[8], Xuedong Xie[8], Junyu Zong[8], Yuwei Shan[9], Yi Guo[1], Marc Willinger[10,11], Hui Wu[12], Qunyang Li[7], Wenlong Wang[2], Peng Gao[6,13], Shiwei Wu[9], Yi Zhang[8,14], Ying Jiang[6,15], Dapeng Yu[16], Enge Wang[5,6,15,17], Xuedong Bai[2]*, Zhu-Jun Wang[10,11]*, Feng Ding[3,4]* & Kaihui Liu[1]*

The development of two-dimensional (2D) materials has opened up possibilities for their application in electronics, optoelectronics and photovoltaics, because they can provide devices with smaller size, higher speed and additional functionalities compared with conventional silicon-based devices[1]. The ability to grow large, high-quality single crystals for 2D components—that is, conductors, semiconductors and insulators—is essential for the industrial application of 2D devices[2–4]. Atom-layered hexagonal boron nitride (hBN), with its excellent stability, flat surface and large bandgap, has been reported to be the best 2D insulator[5–12]. However, the size of 2D hBN single crystals is typically limited to less than one millimetre[13–18], mainly because of difficulties in the growth of such crystals; these include excessive nucleation, which precludes growth from a single nucleus to large single crystals, and the threefold symmetry of the hBN lattice, which leads to antiparallel domains and twin boundaries on most substrates[19]. Here we report the epitaxial growth of a 100-square-centimetre single-crystal hBN monolayer on a low-symmetry Cu (110) vicinal surface, obtained by annealing an industrial copper foil. Structural characterizations and theoretical calculations indicate that epitaxial growth was achieved by the coupling of Cu <211> step edges with hBN zigzag edges, which breaks the equivalence of antiparallel hBN domains, enabling unidirectional domain alignment better than 99 per cent. The growth kinetics, unidirectional alignment and seamless stitching of the hBN domains are unambiguously demonstrated using centimetre- to atomic-scale characterization techniques. Our findings are expected to facilitate the wide application of 2D devices and lead to the epitaxial growth of broad non-centrosymmetric 2D materials, such as various transition-metal dichalcogenides[20–23], to produce large single crystals.

Recently, a macro-sized (with a length of up to 0.5 m) single-crystal Cu (111) foil and the epitaxial growth of single-crystal graphene on that substrate have been demonstrated, paving the way for the epitaxial growth of single crystals of various 2D materials[2,3]. However, the Cu (111) surface is not an appropriate template for the growth of single-crystal hBN owing to the nucleation of antiparallel hBN domains[19]. This is because the epitaxial growth of unidirectionally aligned domains requires the 2D material to adopt the symmetry of the substrate precisely to avoid changes in lattice orientation during a symmetric operation of the substrate. In contrast to graphene, most 2D materials, including hBN, have a lower symmetry (C_{3v} for hBN) and therefore are not compatible with the C_{6v} symmetry of the top-layer atoms of the Cu (111) surface. Thus, the ideal substrate for hBN growth must have C_{3v}, C_3, σ_v or C_1 symmetry. Because the Cu (111) surface cannot be used to grow hBN single crystals, we have to choose a substrate with only σ_v or C_1 symmetry, that is, without a regular low-index face-centred cubic (fcc) surface. To address this challenge, in this study we performed the successful synthesis of a Cu (110) vicinal surface, on which the presence of metal steps along the <211> direction led to a C_1 symmetry. This enabled the coupling of Cu <211> step edges with hBN zigzag edges, resulting in the unidirectional alignment of millions of hBN nuclei over a large 10 × 10 cm^2 area.

In our experiment, 10 × 10 cm^2 single-crystal Cu foils of the Cu (110) vicinal surface were prepared by annealing industrial Cu foils using a designed high-temperature (1,060 °C) pre-treatment process before long-time standard annealing treatment (details in Methods and Extended Data Fig. 1a–g). Such a large-area Cu (110) surface can be easily observed by optical imaging after mild oxidization in air (Fig. 1a), because different surfaces form Cu_2O with different oxidization rates and show characteristic colours[24]. The sharp Cu (220) peak in the X-ray diffraction (XRD) pattern in the 2θ scan (Fig. 1b) and the presence of only two peaks at an interval of exactly 180° in the ϕ scan (Fig. 1c; fixed along Cu <100>) unambiguously confirmed that the single-crystal foil had no in-plane rotation (2θ is the angle between the incident X-rays and the detector and ϕ is the in-plane rotation angle of the sample). Furthermore, at different positions (as marked in Extended Data Fig. 2a), electron backscatter diffraction (EBSD) maps (Fig. 1d, Extended Data Fig. 2b, c), low-energy electron diffraction (LEED) patterns (Fig. 1e, Extended Data Fig. 2d) and scanning transmission electron microscopy (STEM) images (Fig. 1f) revealed the single-crystal nature of the Cu (110) substrate. Here, we note that the exact surface index and the deviation of the tilt angle from ideal Cu (110) is difficult to observe, which means that the tilt angle is smaller than the experimental accuracy of about 1°. We have chosen, however, to call the substrate Cu (110) unless otherwise specified.

Using the Cu foil single crystal as the substrate, 2D hBN was synthesized by a low-pressure chemical vapour deposition (CVD) method with ammonia borane (H_3B-NH_3) as the feedstock (details in Methods and Extended Data Fig. 1h). X-ray photoelectron spectroscopy (XPS), Raman spectroscopy, ultraviolet-visible absorption spectroscopy

---

[1] State Key Laboratory for Mesoscopic Physics, Collaborative Innovation Center of Quantum Matter, School of Physics, Peking University, Beijing, China. [2] Beijing National Laboratory for Condensed Matter Physics, Institute of Physics, Chinese Academy of Sciences, Beijing, China. [3] Centre for Multidimensional Carbon Materials, Institute for Basic Science, Ulsan, South Korea. [4] School of Materials Science and Engineering, Ulsan National Institute of Science and Technology, Ulsan, South Korea. [5] Songshan Lake Laboratory for Materials Science, Dongguan, China. [6] International Center for Quantum Materials, School of Physics, Peking University, Beijing, China. [7] Department of Engineering Mechanics, State Key Laboratory of Tribology, Tsinghua University, Beijing, China. [8] National Laboratory of Solid State Microstructure, School of Physics, Nanjing University, Nanjing, China. [9] State Key Laboratory of Surface Physics, Key Laboratory of Micro and Nano Photonic Structures (MOE), Department of Physics, Fudan University, Shanghai, China. [10] Scientific Centre for Optical and Electron Microscopy, Eidgenössische Technische Hochschule Zürich, Zürich, Switzerland. [11] Department of Inorganic Chemistry, Fritz Haber Institute of Max Planck Society, Berlin, Germany. [12] State Key Laboratory of New Ceramics, Fine Processing School of Materials Science and Engineering, Tsinghua University, Beijing, China. [13] Electron Microscopy Laboratory, School of Physics, Peking University, Beijing, China. [14] Collaborative Innovation Center of Advanced Microstructures, Nanjing University, Nanjing, China. [15] Center for Excellence in Topological Quantum Computation, University of Chinese Academy of Sciences, Beijing, China. [16] Shenzhen Key Laboratory of Quantum Science and Engineering, Department of Physics, South University of Science and Technology of China, Shenzhen, China. [17] Physical Science Laboratory, Huairou National Comprehensive Science Center, Beijing, China. [18] These authors contributed equally: Li Wang, Xiaozhi Xu, Leining Zhang, Ruixi Qiao. *e-mail: xdbai@iphy.ac.cn; zhujun.wang@scopem.ethz.ch; f.ding@unist.ac.kr; khliu@pku.edu.cn

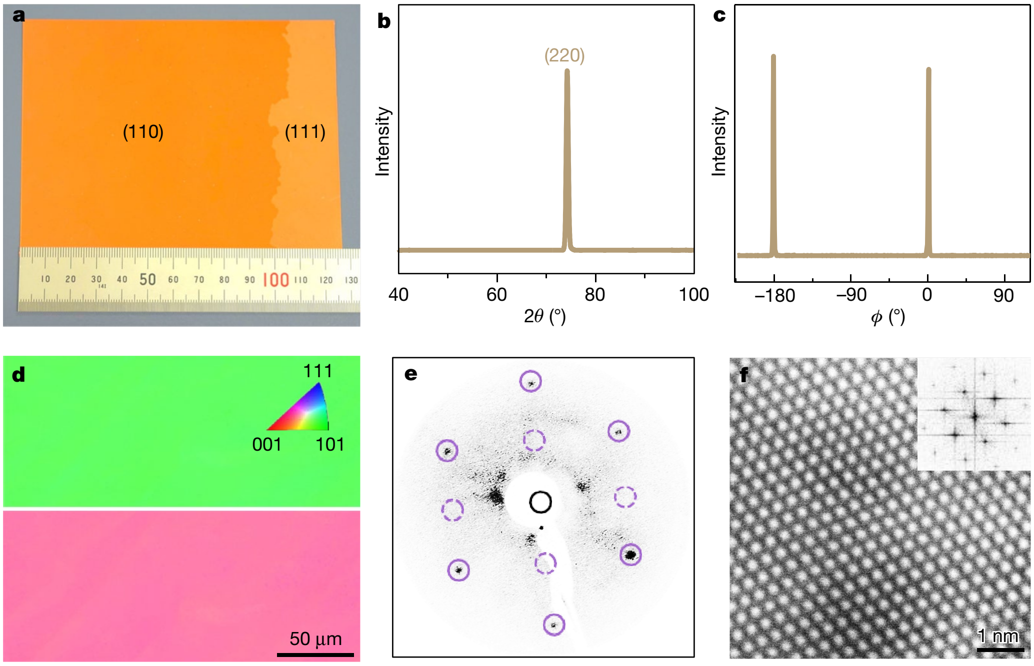

Fig. 1 | Characterization of single-crystal Cu (110) obtained by annealing an industrial Cu foil. a, Optical image of the as-annealed Cu foil after mild oxidation in air. Owing to their different oxidation rates, the Cu (110) and Cu (111) domains have a different thickness of Cu_2O on their surfaces and are therefore different colours. Typical Cu (110) single crystals with areas of 10 × 10 cm^2 were obtained. **b**, **c**, XRD patterns obtained by a 2θ scan of the Cu (110) foil (**b**) and a ϕ scan fixed along the Cu <100> direction (**c**), confirming the single-crystal nature of the Cu (110) foil, without in-plane rotation. **d**, Representative EBSD maps of as-annealed Cu (110) foils (upper panel, along the [001] direction; lower panel, along the [010] direction) measured at position 1 shown in Extended Data Fig. 2a. **e**, Representative LEED pattern of as-annealed Cu (110) foils measured at position 1 shown in Extended Data Fig. 2a. The purple solid and dashed circles correspond to the visible and invisible diffraction points (due to the extinction rule), respectively. **f**, Atomically resolved STEM image of as-annealed Cu (110) foils. Inset, fast Fourier transformation (FFT) pattern of the STEM image. The results of these characterization experiments prove that the as-annealed Cu foil is a single-crystal Cu (110) foil with an area of 10 × 10 cm^2.

(UV-Vis), atomic force microscopy (AFM) and STEM were used to confirm that the as-grown sample was a 2D hBN monolayer (Extended Data Fig. 3). The SEM images showed a striking result: the hBN domains grown on the Cu (110) surface were all triangular, with their domains aligned unidirectionally on the Cu foil surface at the centimetre scale. The proportion of aligned domains was estimated to be about 99.5% (Fig. 2a, Extended Data Fig. 4a). To confirm that the aligned domains had the same crystalline orientation, we performed LEED measurements. LEED patterns (Fig. 2b, Extended Data Fig. 4b) measured at multiple positions (marked in Extended Data Fig. 2a) confirmed that the crystalline lattice of the hBN domains were aligned in the same direction[14]. The unidirectional alignment of the hBN lattice was further proven by polarized second-harmonic generation (SHG) mapping[25], where a dark boundary line was observed between hBN lattices of different domains when these were not aligned (Extended data Fig. 5a). As shown in Fig. 2c, no boundary line was observed in the bulk area of coalescence of hBN domains, which also indicates a similar crystalline orientation for the two coalesced grains.

During the growth of a 2D material on a Cu surface, seamless stitching is expected in the coalescence area of two unidirectionally aligned grains because the perfect single-crystal lattice is always the most stable structure, as has been proven by the CVD growth of graphene[2,3]. To further confirm the seamless stitching of hBN domains, hydrogen (H_2) etching was employed to visualize the different possible boundaries on the macroscopic scale[3,4]. Figure 2d and Extended Data Fig. 5b show no etching line between unidirectionally aligned hBN domains; by contrast, for domains with different alignments, the etched boundary is clearly visualized (Fig. 2e, Extended Data Fig. 5c). Ultraviolet-light oxidization was also carried out to expose possible grain boundaries, when present[2,3]. Similar results were obtained, leading us to the conclusion that the large-area hBN film was a single crystal (Extended Data Fig. 5d, e). High-resolution transmission electron microscopy (HRTEM) was used to characterize the quality of the stitching line between domains on the atomic scale. The as-grown hBN samples were transferred onto specially constructed single-crystal graphene TEM grids to observe the moiré patterns in the hBN/graphene heterostructure. It is well known that even a small difference in the rotation angle can lead to a dramatic change in the moiré pattern. Consistent moiré patterns were collected at multiple places around the concave corner in the joint area of two unidirectionally aligned hBN domains (shown in Fig. 2f, g, Extended Data Fig. 6a–l), whereas a clear difference in the moiré pattern and an obvious grain boundary were observed in the area of confluence of two misaligned hBN domains (Extended Data Fig. 6m–p). The above verifications confirm that our unidirectionally aligned hBN domains can be seamlessly stitched into an intact piece of single-crystal film. Further angle-resolved photoemission spectroscopy (ARPES) spectra also revealed that the hBN film was high-quality single crystal (Extended Data Fig. 7).

We further used environmental scanning electron microscopy (SEM) to study the growth dynamics in situ and to understand the kinetics of the epitaxial growth of unidirectional hBN domains on Cu (110). Our in situ observations suggested that our Cu (110) single-crystal substrate is 'vicinal' because of the existence of steps and that the step edges play a crucial role in the unidirectional alignment of hBN domains. SEM images (Fig. 3a, b) confirmed that each hBN single crystal was nucleated near a step edge, with one edge of the single crystal tightly attached to the upward side of the step edge during the growth process, and the single crystal propagated rapidly on the plateau between neighbouring step edges. Once one of its edges reached a neighbouring step edge in the downward direction, the propagation of the edge was arrested temporarily[26,27]. Our in situ observation thus clearly confirmed that the unidirectional alignment of the hBN domains was caused by step-edge-mediated nucleation, and the truncated shape of the hBN domains was a consequence of the high energy barriers of a hBN edge

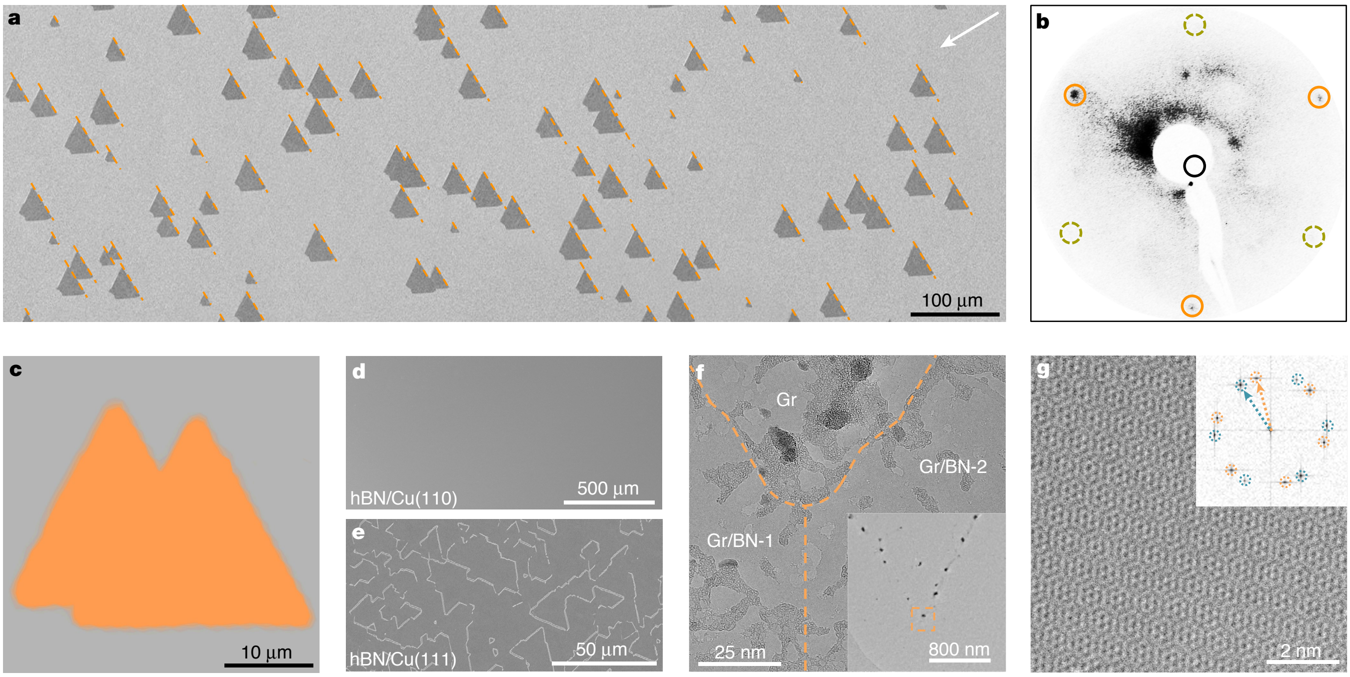

Fig. 2 | Unidirectional alignment and seamless stitching of hBN domains on Cu (110). **a**, SEM image of as-grown unidirectionally aligned hBN domains on the Cu (110) substrate (the arrow on the top right corner points to the downward growth direction of domains). **b**, Representative LEED pattern of as-grown hBN samples measured at position 1 shown in Extended Data Fig. 2a. Because of the triple symmetry, three diffraction points have higher intensity (solid orange circles) than the other three (dashed green circles). The black circle shows the original point in the reciprocal space. **c**, Polarized SHG mapping of two unidirectionally aligned hBN domains. The uniform colour without boundary lines demonstrates that the aligned hBN domains have the same lattice orientation. **d**, **e**, SEM images of as-grown hBN films after H_2 etching at 1,000 °C for 30 min. No boundaries are observed for the hBN film grown on Cu (110) (**d**), but obvious boundaries can be observed on Cu (111) (**e**). **f**, Low-magnification TEM image obtained at the concave corner in the area of confluence of aligned hBN domains on a monolayer single-crystal graphene (Gr) support. Shown are two partially merged hBN domains (BN-1 and BN-2) transferred onto the graphene films. The inset shows the same image at a lower magnification. **g**, Representative HRTEM image showing a uniform moiré pattern at the concave corner in the joint area between two unidirectionally aligned hBN domains. Inset, FFT patterns. The orange (blue) arrow points to the diffraction pattern of hBN (graphene).

passing over a step edge of the metal surface in the upward and the downward direction. Because of the presence of parallel (bunched) step edges (from the uniform surface tilt angle) on the single-crystal vicinal Cu (110) surface (see ex situ AFM images in Extended Data Fig. 8a), this growth kinetics led to unidirectionally aligned hBN domains (Fig. 3c, Extended Data Fig. 8b–g). The growth process is schematically illustrated in Fig. 3d.

The AFM phase image in Fig. 4a shows that the parallel (bunched) step edges of the Cu (110) surface are also parallel to the longest edge of the truncated triangular hBN single crystal, and the scanning tunnelling microscopic (STM) image in Fig. 4b clearly reveals that the longest hBN edge is a zigzag edge. By further comparing the reciprocal lattice information of hBN and Cu (110) (Fig. 4c, d), we find that all the Cu step edges are along the <211> direction (schematically shown in Fig. 4e

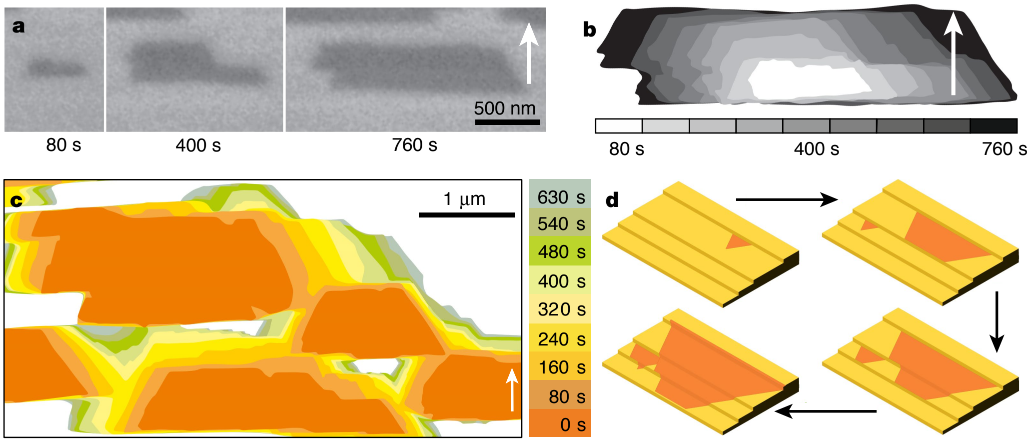

Fig. 3 | In situ observation of the unidirectional growth of hBN domains. **a**, In situ SEM images of a hBN domain, probably formed from a nucleation centre at the surface steps, at different growth times. **b**, Superposition of images showing the areal growth of the domain in **a**. **c**, Shape evolution of several hBN domains, reproduced as a colour-coded superposition of outlines extracted from images recorded during 700 s. **d**, Schematic diagrams highlighting the unidirectional growth of hBN domains and the anisotropic growth speed on a Cu surface with steps. The arrows in **a**–**c** point to the downward growth direction of domains.

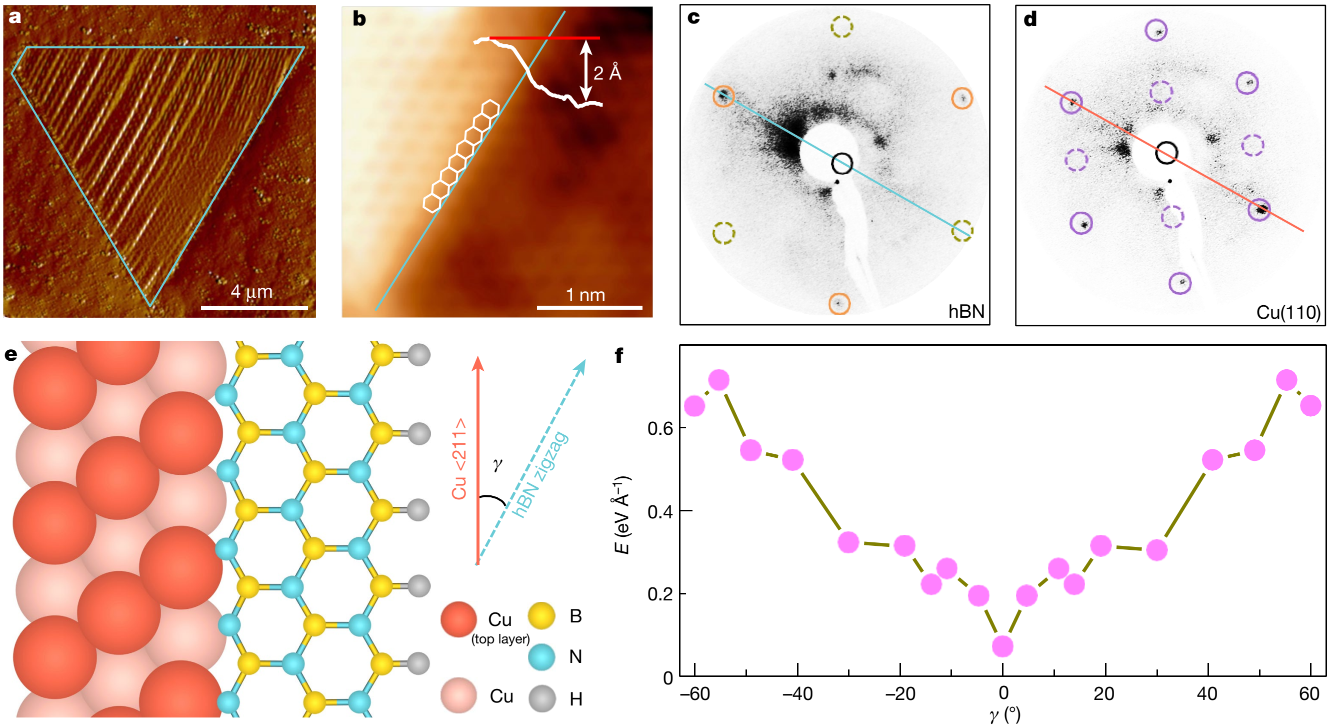

Fig. 4 | Mechanism of edge-coupling-guided epitaxial growth of hBN domains on Cu (110). **a**, AFM phase image of a hBN domain on Cu (110), showing that one edge of the hBN domain is parallel to the surface steps. **b**, Atomic-resolution STM image of a hBN domain covering the Cu (110) plateaus both upwards and downwards, showing the zigzag edge of hBN aligned parallel to the atomic step (blue line) on the Cu surface. Here, the white curve shows the height profile of the Cu step; the height of the plateau is 2 Å. **c**, **d**, LEED patterns of as-grown hBN domains and the underlying Cu (110) surface measured at position 1 in Extended Data Fig. 2a. The blue line in **c** corresponds to the zigzag direction of the hBN lattice in real space and the red line in **d** to the <211> direction of Cu in real space. The purple solid and dashed circles in **d** correspond to the visible and invisible diffraction points (due to the extinction rule), respectively. **e**, Schematic diagrams of the configuration of the hBN lattice and the atomic step on Cu (110), obtained from the STM and LEED data in **b**–**d**. γ is the angle between Cu <211> and the zigzag direction in the hBN lattice; $\gamma = 0°$ for the atomic model in **e**. **f**, First-principles DFT calculations of the formation energies of various hBN edges attached to a Cu <211> step on the Cu (110) substrate. The results show that the system is energetically favoured for $\gamma = 0°$ owing to the coupling between the Cu <211> step edge and the hBN zigzag edge (details in Methods).

and Extended Data Fig. 9). To confirm this edge-coupling-guided growth theoretically, we carried out ab initio calculations based on the experimentally obtained structural information. The formation energy for hBN growing on Cu (110) with steps along Cu <211> has a single minimum-energy state at $\gamma = 0°$ (shown in Fig. 4f), where γ is the angle between the Cu <211> direction and the zigzag direction of the hBN nucleus (Fig. 4e). In practice, step edges might not be perfectly straight. A step edge slightly deviating from Cu <211> can be perceived as many short segments of the Cu <211> step edge connected by atomic-sized kinks. As reported in a recent study, the complementary counter-kinks of the hBN edge are likely to appear at (and compensate for the kinks of) the metal step edges, and thus ensure the unidirectionally aligned growth of hBN domains[28]. In addition, $\gamma = 0°$ is one of the most energetically preferred orientations between the hBN lattice and the Cu (110) facet, which indicates that interfacial coupling may also contribute to the epitaxy. Considering these results, the edge-coupling-guided growth mechanism has wide applicability and high repeatability. For example, unidirectionally aligned growth of hBN domains could be also observed on the Cu (410) facet (Extended Data Fig. 10a); however, randomly aligned hBN domains were frequently observed on the Cu (100) facet (Extended Data Fig. 10b), whereas anti-parallel domains were often obtained on the Cu (111) facet (Extended Data Fig. 10c).

In summary, single-crystal hBN films with areas of 10 × 10 cm^2 (three orders of magnitude larger than those grown previously), were synthesized on a large-area single-crystal Cu (110) foil by annealing regular, industrially produced Cu foils. The easy preparation of the Cu substrate implies the immediate availability and wide applicability of single-crystal 2D hBN films. Moreover, the observed edge-coupling-guided growth mechanism on a vicinal surface is expected to be applicable to all non-centrosymmetric 2D materials, which will enable the growth of large-area single crystals of such materials and facilitate their use in different applications in the near future.

Note added in proof: After the submission of our manuscript, two studies related to the growth of single-crystal hBN were reported by other researchers[28,29].

Online content

Any methods, additional references, Nature Research reporting summaries, source data, extended data, supplementary information, acknowledgements, peer reviewinformation; details of author contributions and competing interests; and statements of data and code availability are available at https://doi.org/10.1038/s41586-019-1226-z.

Received: 22 October 2018; Accepted: 28 March 2019;
Published online 22 May 2019.

1. Novoselov, K. S., Mishchenko, A., Carvalho, A. & Neto, A. H. C. 2D materials and van der Waals heterostructures. *Science* **353**, aac9439 (2016).
2. Nguyen, V. L. et al. Seamless stitching of graphene domains on polished copper (111) foil. *Adv. Mater.* **27**, 1376–1382 (2015).
3. Xu, X. Z. et al. Ultrafast epitaxial growth of metre-sized single-crystal graphene on industrial Cu foil. *Sci. Bull.* **62**, 1074–1080 (2017).
4. Vlassiouk, I. V. et al. Evolutionary selection growth of two-dimensional materials on polycrystalline substrates. *Nat. Mater.* **17**, 318–322 (2018).
5. Yang, W. et al. Epitaxial growth of single-domain graphene on hexagonal boron nitride. *Nat. Mater.* **12**, 792–797 (2013).
6. Dean, C. R. et al. Hofstadter's butterfly and the fractal quantum Hall effect in moiré superlattices. *Nature* **497**, 598–602 (2013).
7. Hunt, B. et al. Massive Dirac fermions and Hofstadter butterfly in a van der Waals heterostructure. *Science* **340**, 1427–1430 (2013).

8. Wang, E. Y. et al. Gaps induced by inversion symmetry breaking and second-generation Dirac cones in graphene/hexagonal boron nitride. *Nat. Phys.* **12**, 1111–1115 (2016).
9. Watanabe, K., Taniguchi, T. & Kanda, H. Direct-bandgap properties and evidence for ultraviolet lasing of hexagonal boron nitride single crystal. *Nat. Mater.* **3**, 404–409 (2004).
10. Tran, T. T. et al. Quantum emission from hexagonal boron nitride monolayers. *Nat. Nanotechnol.* **11**, 37–41 (2016).
11. Hu, S. et al. Proton transport through one-atom-thick crystals. *Nature* **516**, 227–230 (2014).
12. Wang, L. et al. One-dimensional electrical contact to a two-dimensional material. *Science* **342**, 614–617 (2013).
13. Liu, Z. et al. In-plane heterostructures of graphene and hexagonal boron nitride with controlled domain sizes. *Nat. Nanotechnol.* **8**, 119–124 (2013).
14. Liu, L. et al. Heteroepitaxial growth of two-dimensional hexagonal boron nitride templated by graphene edges. *Science* **343**, 163–167 (2014).
15. Kim, S. M. et al. Synthesis of large-area multilayer hexagonal boron nitride for high material performance. *Nat. Commun.* **6**, 8662 (2015).
16. Li, J. D. et al. Growth of polar hexagonal boron nitride monolayer on nonpolar copper with unique orientation. *Small* **12**, 3645–3650 (2016).
17. Lu, G. Y. et al. Synthesis of large single-crystal hexagonal boron nitride grains on Cu–Ni alloy. *Nat. Commun.* **6**, 6160 (2015).
18. Wang, L. F. et al. Water-assisted growth of large-sized single crystal hexagonal boron nitride grains. *Mater. Chem. Front.* **1**, 1836–1840 (2017).
19. Song, X. J. et al. Chemical vapor deposition growth of large-scale hexagonal boron nitride with controllable orientation. *Nano Res.* **8**, 3164–3176 (2015).
20. Kang, K. et al. High-mobility three-atom-thick semiconducting films with wafer-scale homogeneity. *Nature* **520**, 656–660 (2015).
21. Fu, D. Y. et al. Molecular beam epitaxy of highly crystalline monolayer molybdenum disulfide on hexagonal boron nitride. *J. Am. Chem. Soc.* **139**, 9392–9400 (2017).
22. Zhou, J. D. et al. A library of atomically thin metal chalcogenides. *Nature* **556**, 355–359 (2018).
23. Sahoo, P. K. et al. One-pot growth of two-dimensional lateral heterostructures via sequential edge-epitaxy. *Nature* **553**, 63–67 (2018).
24. Zhang, Z. et al. Identification of copper surface index by optical contrast. *Adv. Mater. Interfaces* **5**, 1800377 (2018).
25. Cheng, J. X. et al. Kinetic nature of grain boundary formation in as-grown MoS_2 monolayers. *Adv. Mater.* **27**, 4069–4074 (2015).
26. Sutter, P., Cortes, R., Lahiri, J. & Sutter, E. Interface formation in monolayer graphene–boron nitride heterostructures. *Nano Lett.* **12**, 4869–4874 (2012).
27. Yi, D. et al. What drives metal-surface step bunching in graphene chemical vapor deposition? *Phys. Rev. Lett.* **120**, 246101 (2018).
28. Bets, K. V., Gupta, N. & Yakobson, B. I. How the complementarity at vicinal steps enables growth of 2D monocrystals. *Nano Lett.* **19**, 2027–2031 (2019).
29. Lee, J. S. et al. Wafer-scale single-crystal hexagonal boron nitride film via self-collimated grain formation. *Science* **362**, 817–821 (2018).

Acknowledgements This work was supported by the National Key R&D Program of China (2016YFA0300903, 2016YFA0300804 and 2018YFA0306800), the Natural Science Foundation of China (11888101, 51522201, 11474006, 11714154, 11634001 and 21725302), the National Equipment Program of China (ZDYZ2015-1), the Beijing Municipal Science & Technology Commission (Z181100004218006), the Beijing Graphene Innovation Program (Z181100004818003), the Science, Technology and Innovation Commission of Shenzhen Municipality (ZDSYS20170303165926217 and JCYJ20170412152620376), the Guangdong Innovative and Entrepreneurial Research Team Program (2016ZT06D348), the Bureau of Industry and Information Technology of Shenzhen (graphene platform contract number 201901161512), the National Postdoctoral Program for Innovative Talents (BX201700014), the Strategic Priority Research Program of CAS (XDB28000000), the National Program for Thousand Young Talents of China and the Institute for Basic Science of South Korea (IBS-R019-D1).

Reviewer information *Nature* thanks Kian Ping Loh and Boris I. Yakobson and the other anonymous reviewer(s) for their contribution to the peer review of this work.

Author contributions K.L., E.W., D.Y. and L.W. conceived the project. K.L. supervised the project. L.W., X. Xu, M. Wu, Zhihong Zhang, Zhibin Zhang and W.W. conducted the annealing of the single-crystal Cu foil and ex situ growth of single-crystal hBN. F.D. and L.Z. performed the theoretical calculations. Z.-J.W. and M. Willinger performed the in situ growth experiments. X.B., R.Q., L.W., Y.G. and P.G. performed the transfer of hBN and the TEM experiments. L.W. and X. Xu performed the EBSD, UV-Vis and LEED measurements, as well as the etching and oxidization experiments. Y.J. and Z.W. performed the STM experiments. Y.Z., W.C., X. Xie and J.Z. performed the ARPES measurements. S.W., J.L. and Y.S. performed the polarized SHG mapping measurements. Q.L., Zhihong Zhang and S.Z. performed the AFM measurement. All of the authors discussed the results and wrote the paper.

Competing interests The authors declare no competing interests.

Additional information

Extended data is available for this paper at https://doi.org/10.1038/s41586-019-1226-z.

Reprints and permissions information is available at http://www.nature.com/reprints.

Correspondence and requests for materials should be addressed to X.B., Z.-J.W., F.D. or K.L.

METHODS

Annealing of a 10 × 10 cm^2 single-crystal Cu (110) foil. A commercially available polycrystalline Cu foil (25 μm thick, 99.8%; Sichuan Oriental Stars Trading Co. Ltd) was loaded into a tube furnace with a chamber of diameter 23 cm and length 50 cm (Kejing Co. Ltd). The foil was first annealed at 1,060 °C (where the Cu surface started to melt) for 2–10 min under a mixed-gas flow (Ar, 500 sccm, H_2, 50 sccm; sccm, standard cubic centimetres per minute) at atmospheric pressure, and then the temperature was quickly decreased to 1,040 °C and the Cu foil was annealed at this temperature for 3 h. For the subsequent annealing, a small piece of as-annealed single-crystal Cu (110) foil with steps along Cu <211> was placed on the surface of a raw polycrystalline Cu foil as an artificial seed, which enhanced the yield of the single-crystal Cu (110) foil with the steps along Cu <211> to a great extent. To identify the surface index, the as-annealed Cu foil was heated in a box furnace (Tianjin Kaiheng Co. Ltd, custom-designed) at 120 °C for 1 h.

Growth of 10 × 10 cm^2 single-crystal 2D hBN films. The precursor ammonia borane (97%; Aldrich) was filled into an Al_2O_3 crucible and placed at a distance of 1 m from the single-crystal Cu (110) foil substrate. First, the substrate was heated to the growth temperature (1,035 °C) under a mixed-gas flow (Ar, 500 sccm; H_2, 50 sccm) at atmospheric pressure. The CVD system was then switched to low pressure (about 200 Pa) with Ar (5 sccm) and H_2 (45 sccm), while the precursor was heated to 65 °C within 10 min using a heating band. To visualize the individual hBN domains, the growth time was fixed at 1 h; a continuous hBN film was obtained after 3 h of growth. For imaging grain boundaries, when present, the as-grown hBN film was etched at 1,000 °C for 30 min under H_2 and Ar (Ar, 250 sccm; H_2, 250 sccm) at atmospheric pressure. After growth or etching, the whole CVD system was cooled rapidly to room temperature.

Transfer of hBN films. The as-grown hBN domains were transferred onto 90-nm-thick SiO_2/Si wafers, holey-carbon-film TEM grids (Zhongjingkeyi GIG-1213-3C) and homemade monolayer graphene TEM grids using the polymethyl-methacrylate-based transfer technique. The graphene TEM grids were prepared by transferring large-area monolayer single-crystal graphene on commercial holey-carbon-film TEM grids (Zhongjingkeyi GIG-2010-3C).

In situ CVD growth observed by environmental SEM. In situ CVD growth experiments were performed inside the chamber of a modified environmental SEM system (FEI Quantum 200) with a custom infrared laser heating stage and with gas supplied through a leak valve. The as-grown single-crystal Cu (110) foil was cut into small pieces (5 mm × 5 mm) and annealed at 1,000 °C under H_2 flow (10 sccm) at 25 Pa for 1 h. CVD growth was then carried out at 850–950 °C. Images were recorded by an Everhart–Thornley detector or a large-field detector during CVD growth.

Computational details. The formation energies of the various hBN edges that are attached to the <211> step edge of a Cu (110) surface were calculated using dispersion-corrected density functional theory (DFT) calculations as implemented in the Vienna Ab initio Simulation Package. Exchange-correlation functions were treated using the generalized gradient approximation, and the interaction between valence electrons and ion cores was calculated by the projected augmented wave method. A force lower than 0.01 eV Å^{-1} on each atom with an energy convergence of 10^{-4} eV was used as the criterion for structural relaxation. The formation energy of an edge attached to a <211> step edge of the Cu (110) vicinal surface is defined as $\varepsilon_{\mathrm{edge/Cu}} = \varepsilon_{\mathrm{pri}} - \varepsilon_{\mathrm{B}} = \varepsilon_{\mathrm{pri}} - (E_{\mathrm{Cu}} + E_{\mathrm{hBN}} - E_{\mathrm{T}} - E_{\mathrm{vdW}})/L$, where $\varepsilon_{\mathrm{pri}}$ and ε_{B} are the edge energy of the pristine hBN and the binding energy of a hBN edge attached to a <211> step edge, respectively; E_{Cu}, E_{hBN}, E_{T} and E_{vdW} correspond to the calculated energies of the Cu slab model, the hBN ribbon model, the hBN ribbon attached to the Cu slab and the van der Waals interaction between the hBN ribbon and the Cu slab; and L is the length of the supercell of the calculation. In all DFT calculations, the vacuum spacing between neighbouring images was >12 Å to avoid periodic imaging interaction. The edge energy of a pristine hBN edge is defined as $\varepsilon_{\mathrm{pri}} = \frac{E_2 - E_1 - \Delta N_{\mathrm{BN}}\varepsilon_{\mathrm{BN}} - \Delta N_{\mathrm{N}}\mu_{\mathrm{N}}}{3(L_2 - L_1)}$, where E_2 and E_1 are the energies of two hBN triangles with the same edge configurations but of different size. In this calculation, two triangles with edge length of about 1.5 nm and 2 nm were used. $\varepsilon_{\mathrm{BN}}$ is the energy of a B–N pair in the hBN bulk. $\Delta N_{\mathrm{BN}} = N_{\mathrm{BN2}} - N_{\mathrm{BN1}}$, where N_{BN1} and N_{BN2} are the numbers of B–N pairs of the two hBN triangles. Using N_2 as a reference, $\mu_{\mathrm{N}} = -8.3$ eV is the calculated chemical potential for a nitrogen atom. The van der Waals interaction between the hBN and the Cu (110) surface was calculated by placing a hBN bulk on a Cu (110) slab, with the N zigzag direction along the <211> direction of the substrate. The calculated van der Waals interaction is −0.17 eV per B–N pair. In the calculations of hBN ribbons attached to a Cu surface, the four-atom-thick Cu slab model was used to represent a vicinal Cu (110) surface or a Cu (110) surface with a <211> step, and the models of various hBN ribbons had a width of about 1.0 nm. A maximum strain of less than 3.5% was adopted when building the supercells to calculate the edge energy of hBN on the Cu surface.

Characterization. *Optical measurements.* Raman spectra were obtained with an alpha300R system (WITec, Germany) with a laser excitation wavelength of 532 nm and about 1 mW power. Optical images were obtained using an Olympus BX51 microscope. SHG mapping was done using a customized system equipped with a piezo stage and controller (Physik Instrumente P-333.3CD and E-725), an ultrafast laser (Spectra Physics Inspire ultrafast OPO system; wavelength of 820 nm, pulse duration of 100 fs and repetition rate of 80 MHz) and a grating spectrograph (Princeton SP-2500i). XPS and UV-Vis spectral measurements were performed using an Axis Ultra Imaging X-ray photoelectron spectrometer and a Varian Cary 5000 UV-Vis-NIR spectrophotometer, respectively. ARPES spectra were measured in a setup comprising a SCIENTA DA30L analyser and a monochromatic helium lamp in He I (21.2 eV) mode. The size of the light beam was about 1 mm^2, and the samples were cooled to about 10 K during measurements.

EBSD, LEED, TEM, AFM and STM measurements. EBSD maps were obtained using a PHI 710 scanning Auger nanoprobe. LEED was performed using an Omicron LEED system in ultrahigh vacuum with a base pressure below 3×10^{-7} Pa. STEM/HRTEM experiments were partly performed using FEI Titan Themis G2 300 and JEOL JEM ARM 300CF systems operated at 300 kV and 80 kV, respectively. An atomically resolved STEM image of monolayer hBN was collected using a Nion UltraSTEM 200 instrument operated at 60 kV. AFM images were acquired using a Bruker Dimensional ICON system in ambient atmosphere. STM experiments were performed with a combined nc-AFM/STM system (Createc, Germany) at 77 K with a base pressure below 7×10^{-9} Pa.

Data availability

All related data generated or analysed during the current study are available from the corresponding authors on reasonable request.

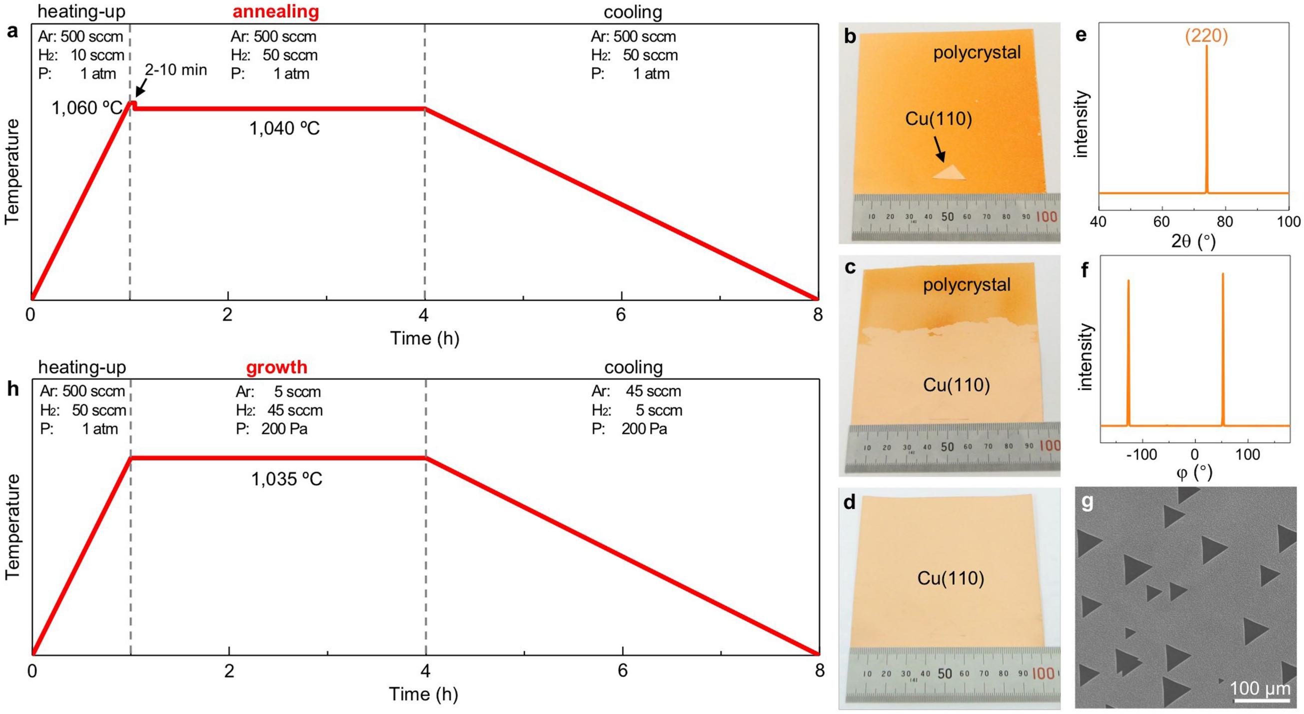

Extended Data Fig. 1 | Annealing protocol for the single-crystal Cu (110) foil and growth of single-crystal hBN. a, Diagram of the annealing procedure used for the single-crystal Cu (110) foil (see Methods for details). **b**, A small piece of single-crystal Cu (110) with <211> steps was placed on a polycrystalline Cu foil of size 10 × 10 cm^2 to guide the annealing of the Cu foil. After annealing at 1,040 °C for 5 min, the nucleus has started to assimilate the polycrystalline Cu foil. **c**, After annealing for 2 h, about three-fifths of the Cu foil was annealed to give a single-crystal Cu foil. **d**, After annealing for 5 h, the entire foil is a single-crystal Cu foil. **e**, **f**, XRD patterns corresponding to a 2θ scan (**e**) and a ϕ scan along the Cu (100) direction (**f**) of as-annealed Cu foil, confirming the single-crystal nature of the Cu (110) foil without in-plane rotation. **g**, SEM image of unidirectionally aligned hBN grown on as-annealed Cu (110). **h**, Diagram of the growth procedure of single-crystal hBN film.

Extended Data Fig. 2 | Characterizations of as-annealed Cu (110) foil at multiple positions. a, Markers 1–9 on the as-annealed Cu foil indicate the positions used for the following characterizations. **b**, **c**, Representative EBSD maps along the [001] (**b**) and [010] (**c**) direction measured at positions 2 ($\mathbf{b}_1$, $\mathbf{c}_1$), 3 ($\mathbf{b}_2$, $\mathbf{c}_2$), 4 ($\mathbf{b}_3$, $\mathbf{c}_3$), 5 ($\mathbf{b}_4$, $\mathbf{c}_4$), 6 ($\mathbf{b}_5$, $\mathbf{c}_5$), 7 ($\mathbf{b}_6$, $\mathbf{c}_6$), 8 ($\mathbf{b}_7$, $\mathbf{c}_7$) and 9 ($\mathbf{b}_8$, $\mathbf{c}_8$). **d**, Representative LEED patterns measured at positions 2 ($\mathbf{d}_1$) to 9 ($\mathbf{d}_8$). The purple solid and dashed circles correspond to the visible and invisible diffraction points (due to the extinction rule), respectively.

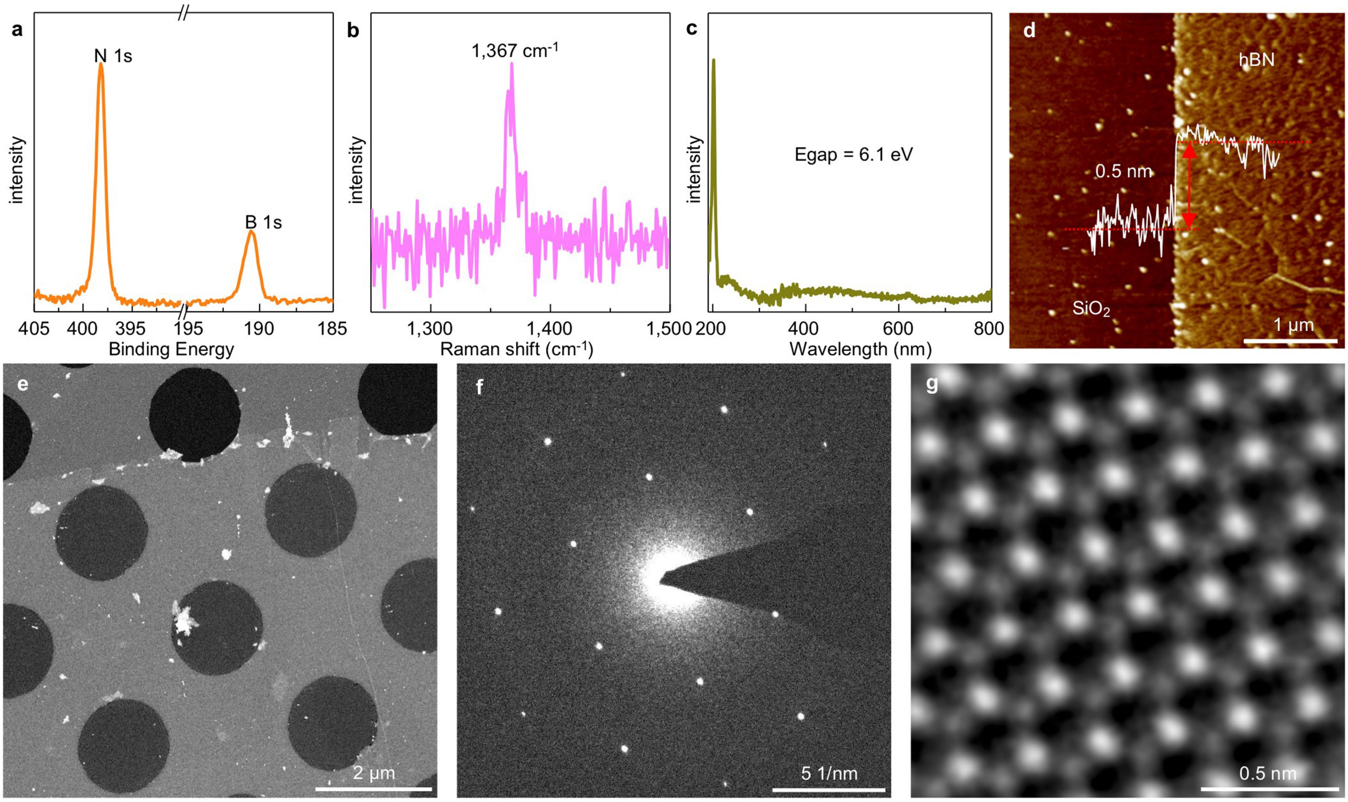

Extended Data Fig. 3 | Characterizations of as-grown hBN samples. **a**, XPS spectra of the hBN film. The characteristic peaks corresponding to N and B confirm the chemical composition of hBN. **b**, Representative Raman spectrum. The characteristic peak at 1,367 cm^{-1} corresponds to the E_{2g} vibration mode of 2D hBN. **c**, UV-Vis absorption spectrum, showing a bandgap of about 6.1 eV. **d**, AFM image of the edge of a hBN domain transferred onto SiO_2/Si, showing monolayer thickness. **e**–**g**, Low-magnification STEM image of a hBN film transferred onto a holey-carbon-film TEM grid (**e**). The SAED pattern (**f**) and atomically resolved HAADF-STEM image (**g**) were collected at the suspended area and show monolayer features.

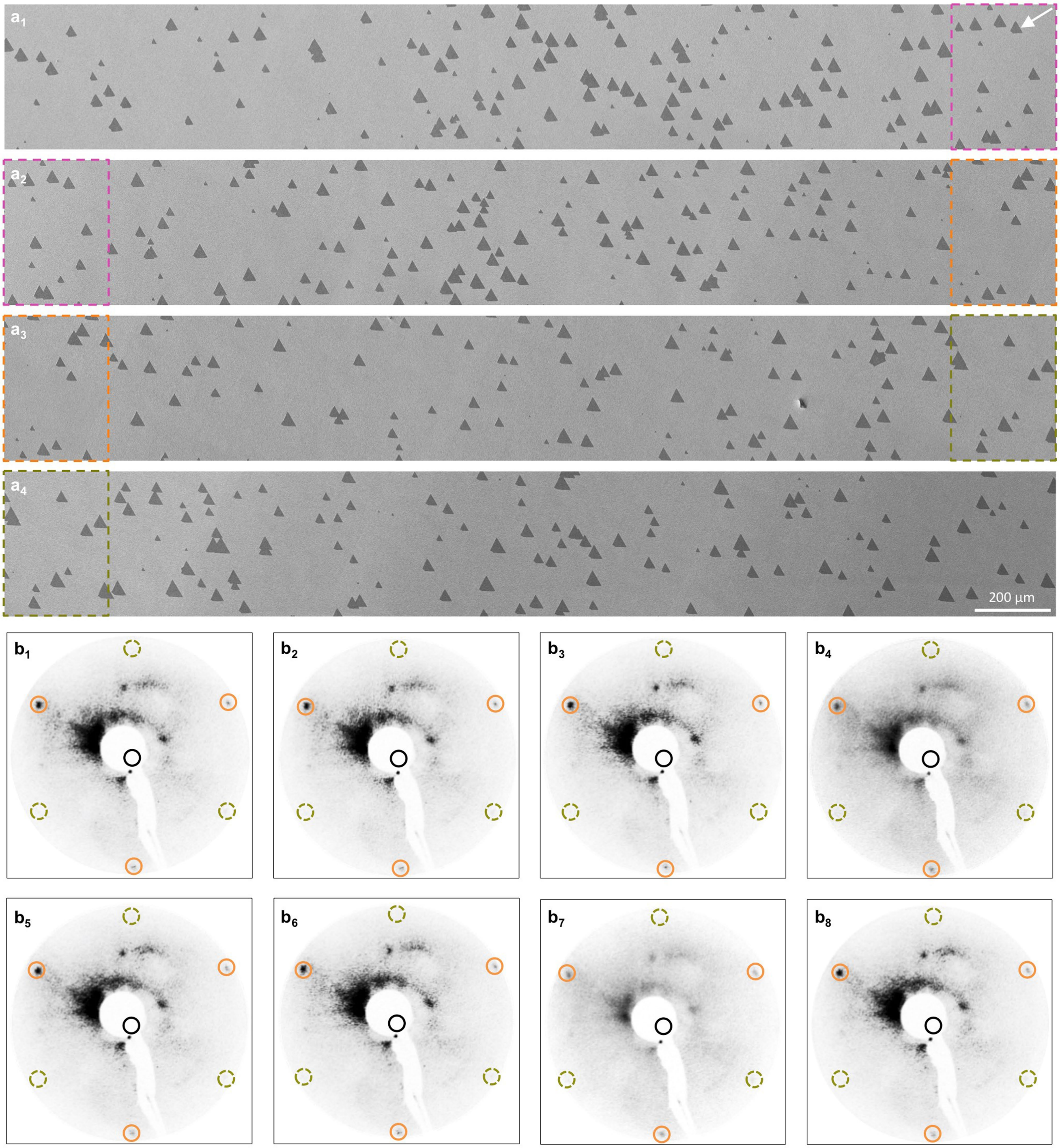

Extended Data Fig. 4 | Unidirectionally aligned growth of hBN domains on Cu (110). **a**, SEM images of hBN domains covering a width of about 1 cm; the overlap regions are marked by same-colour dashed boxes. Among a total of about 700 domains only 3 are not aligned, which indicates that that the unidirectional alignment probability is greater than 99% (the arrow on the upper-right corner points to the downward growth direction of domains). **b**, LEED characterizations at positions 2–9 in Extended Data Fig. 2a.

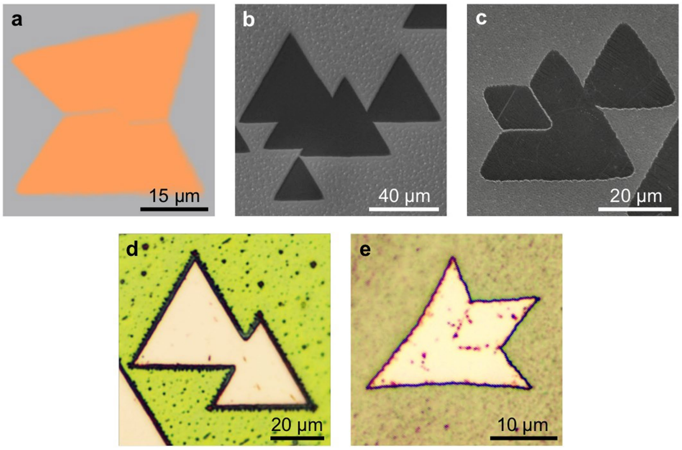

Extended Data Fig. 5 | Boundaries of hBN domains. **a**, Grain boundary between unaligned hBN domains, shown as a dark line in a polarized SHG map. **b**, SEM image of hBN domains grown on Cu (110) after H_2 etching, where no etched lines can be observed. **c**, SEM image of hBN domains grown on Cu (111) with a 60° twist angle after H_2 etching. A clear etched line can be observed. **d**, Optical image of hBN domains grown on Cu (110) after UV oxidation for 30 min, where no boundary line can be observed. **e**, Optical image of hBN domains grown on Cu (111) with a 60° twist angle after UV oxidation for 30 min. Clear oxidation lines can be observed because of the existing boundaries.

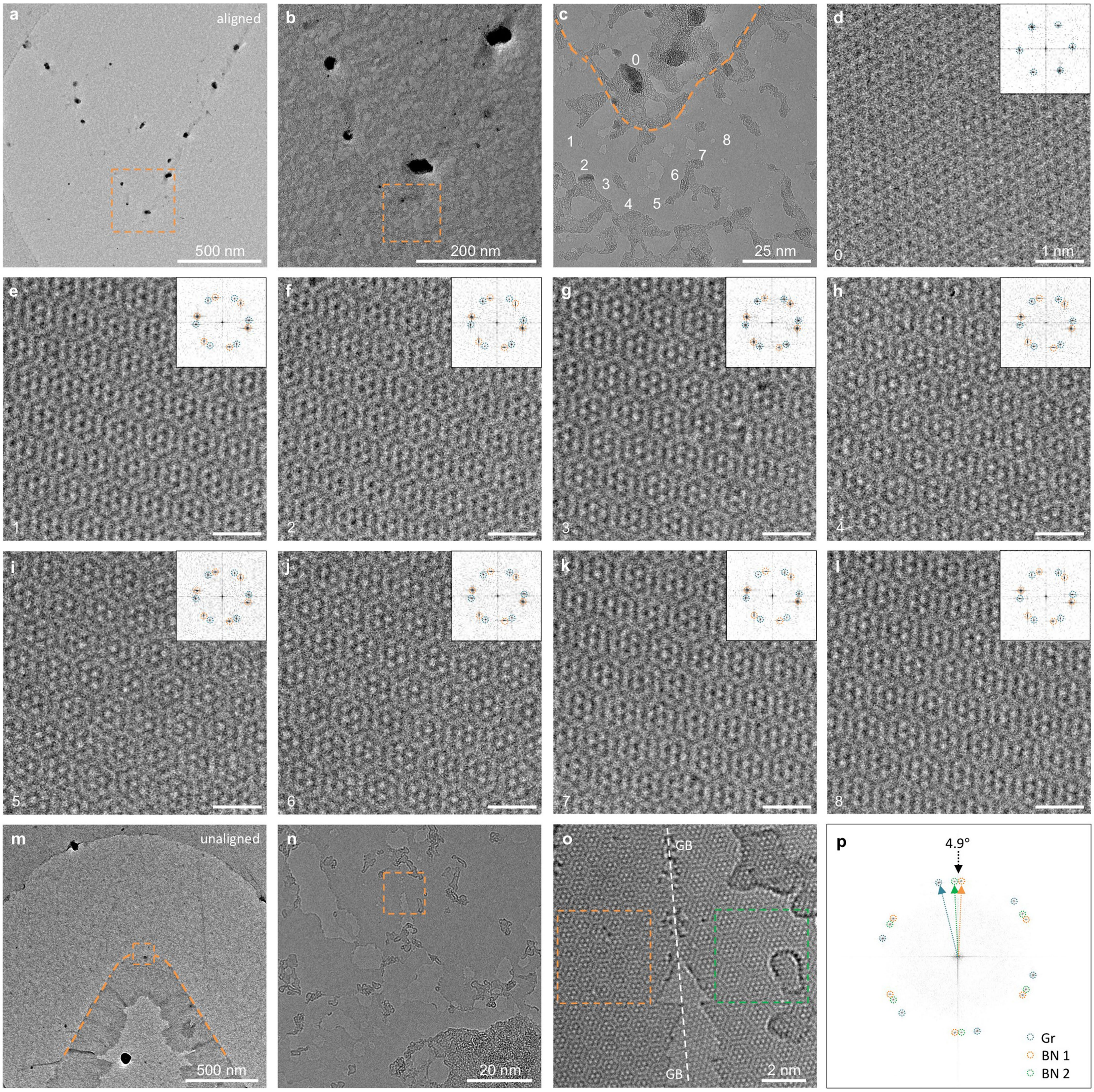

Extended Data Fig. 6 | TEM characterization of the seamless stitching of unidirectionally aligned hBN domains. a–c, TEM images of increasing magnification obtained at the boundary area between two unidirectionally aligned hBN domains on graphene TEM grids. **d–l**, HRTEM images captured at the regions marked by numbers 0–9 in **c**, showing the bare graphene TEM grid at 0 (**d**) and the consistent moiré patterns of monolayer hBN on graphene TEM grids (**e–l**), confirming the seamless stitching of unidirectionally aligned hBN domains without the formation of grain boundaries. The insets show the corresponding FFT patterns. The image sizes of **d–l** are identical. **m–o**, TEM images of increasing magnification at the boundary area between unaligned hBN domains on graphene TEM grids, showing distinct moiré patterns and grain boundary (GB). **p**, FFT pattern of **o**, indicating a twist angle of 4.9° for the two hBN domains.

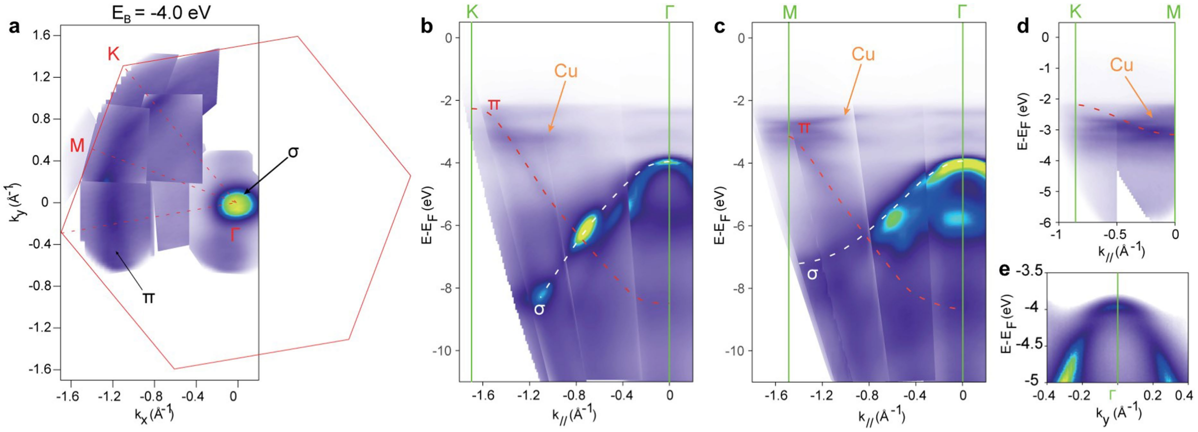

Extended Data Fig. 7 | ARPES spectra of as-grown single-crystal hBN. **a**, Constant-energy mapping at a binding energy of −4.0 eV. The red hexagon indicates the Brillouin zone of hBN (with the high-symmetry points Γ, M and K labelled), in which the top of the σ band located at the Γ point and a section of the π band can be clearly seen. **b**–**d**, ARPES spectra along the K–Γ (**b**), M–Γ (**c**) and K–M (**d**) momentum directions. The white and red dashed curves depict the dispersions of the σ and π band, respectively. The σ band has a strong signal and a very sharp top, whereas the signal from the π band is relatively weak but can still be clearly distinguished. The top of the π band is blended with the bands of the Cu substrate, so it is hard to distinguish. **e**, Magnified ARPES spectrum crossing the Γ point along the k_y direction, as shown in **a**. Here, k_x and k_y denote the momentum components along the horizontal and longitudinal axes of **a**, respectively; $k_{||}$ in **b**, **c** and **d** is oriented along the K–Γ, M–Γ and K–M directions, respectively; $E-E_F$ is the binding energy of band structures; E is the kinetic energy of photoelectrons received by the analyser; and E_F is the Fermi level energy.

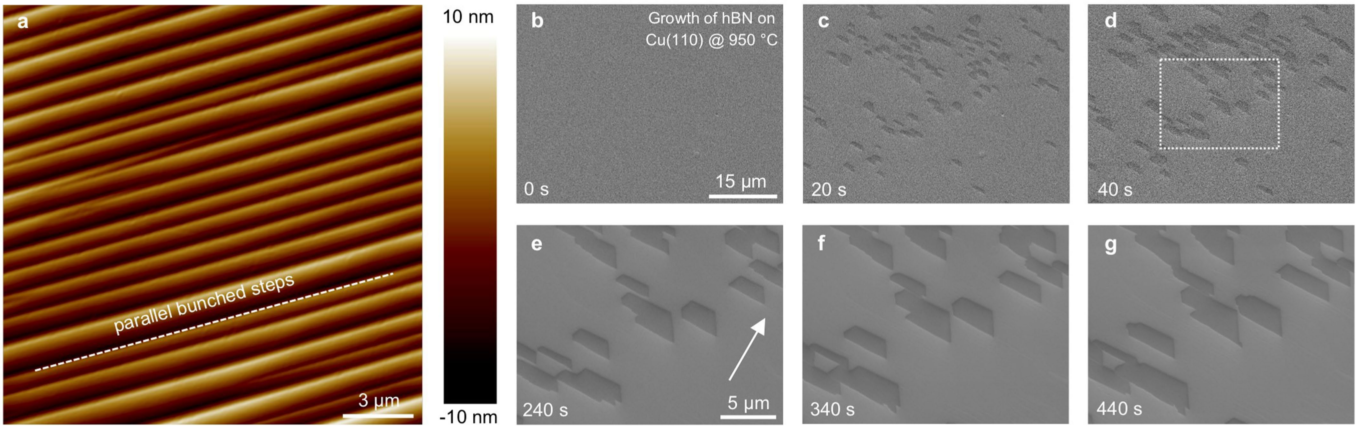

Extended Data Fig. 8 | Evidence of step-edge-guided growth of hBN on Cu (110). **a**, AFM images of parallel bunched steps on a bare as-annealed Cu surface. The average surface roughness is about 3.0 nm (including the bunched steps) and the average roughness of the flat plateaus is about 0.3 nm. **b**–**d**, In situ observation of the hBN growth on Cu (110) at 950 °C. **e**–**g**, Magnified SEM images of the hBN growth on Cu (110) at the area marked by the box in **d**, showing unidirectionally aligned growth of trapezoid hBN domains (the arrow points to the downward growth direction).

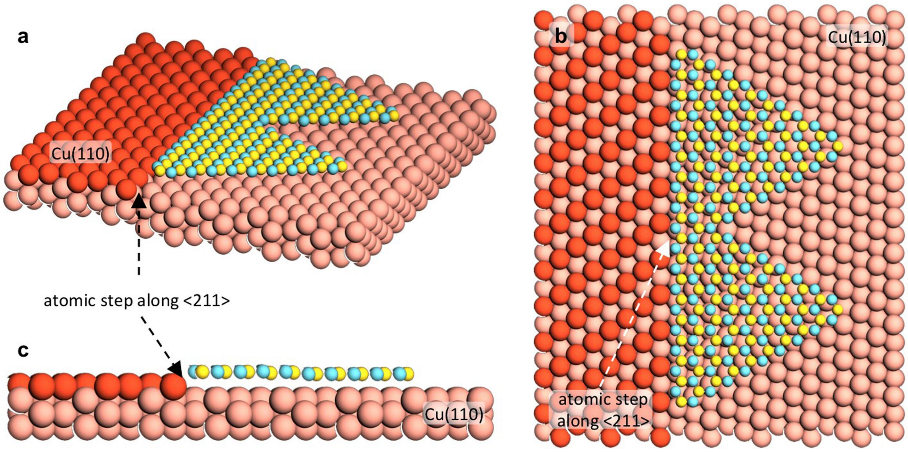

Extended Data Fig. 9 | Edge-coupling-guided hBN growth on Cu (110). a–c, Schematic of edge-coupling-guided hBN growth on a Cu (110) vicinal surface with atomic step edges along the <211> direction. **b** shows the top view and **c** shows the side view of **a**.

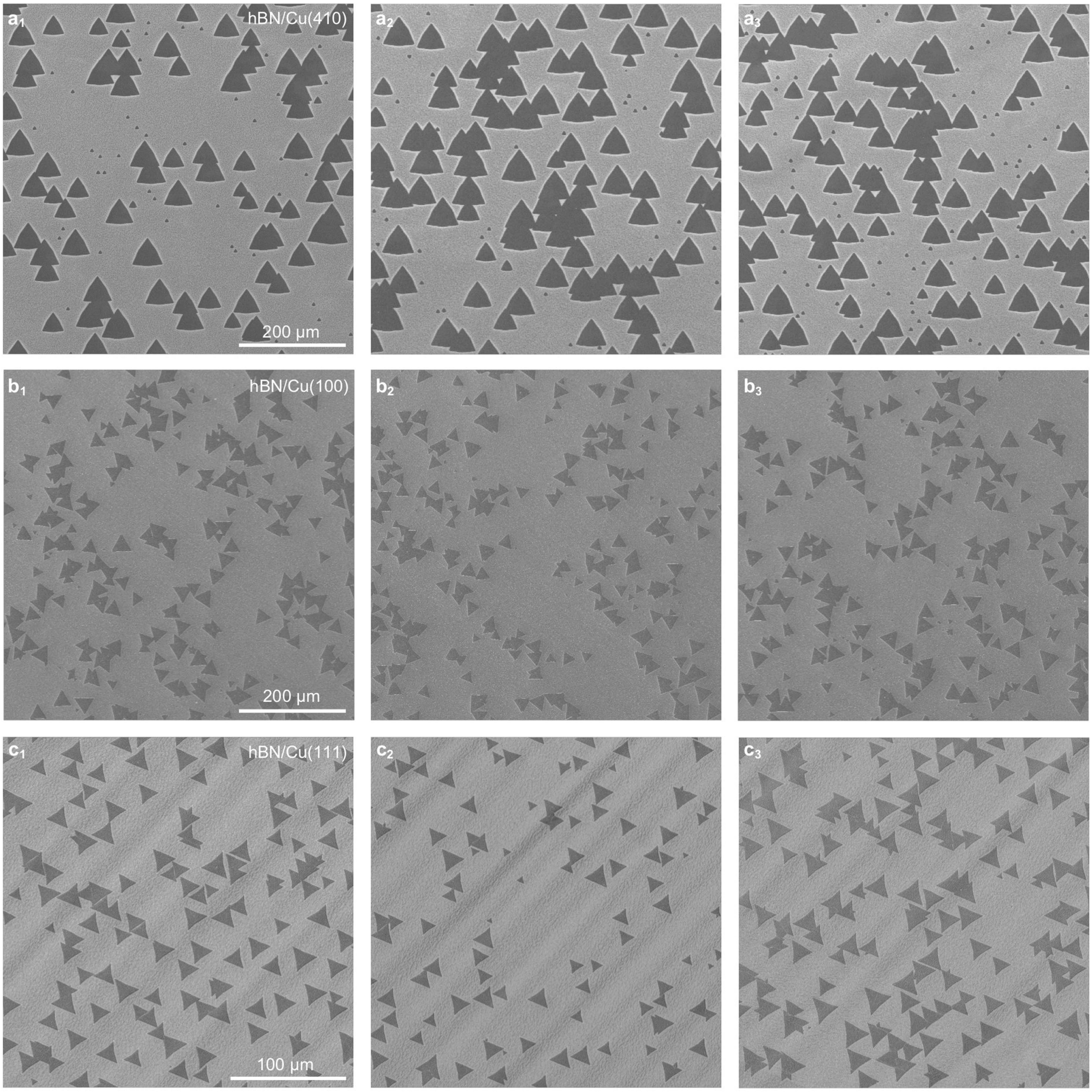

Extended Data Fig. 10 | Growth of hBN domains on different Cu facets. a, SEM images of unidirectionally aligned hBN domains on Cu (410). **b**, SEM images of twisted hBN domains on Cu (100). **c**, SEM images of hBN domains with antiparallel alignment on Cu (111).